

A Continuous Tensor Field Approximation of Discrete DT-MRI Data for Extracting Microstructural and Architectural Features of Tissue

Sinisa Pajevic,* Akram Aldroubi,† and Peter J. Basser‡¹

*MSCL, CIT; ‡STBB, NICHD, National Institutes of Health, Bethesda, Maryland 20892-5772; and †Department of Mathematics, Vanderbilt University, Nashville, Tennessee 37203

Received July 5, 2000; revised September 26, 2001

The effective diffusion tensor of water, \mathbf{D} , measured by diffusion tensor MRI (DT-MRI), is inherently a discrete, noisy, voxel-averaged sample of an underlying macroscopic effective diffusion tensor field, $\mathbf{D}(\mathbf{x})$. Within fibrous tissues this field is presumed to be continuous and smooth at a gross anatomical length scale. Here a new, general mathematical framework is proposed that uses measured DT-MRI data to produce a continuous approximation to $\mathbf{D}(\mathbf{x})$. One essential finding is that the continuous tensor field representation can be constructed by repeatedly performing one-dimensional B-spline transforms of the DT-MRI data. The fidelity and noise-immunity of this approximation are tested using a set of synthetically generated tensor fields to which background noise is added via Monte Carlo methods. Generally, these tensor field templates are reproduced faithfully except at boundaries where diffusion properties change discontinuously or where the tensor field is not microscopically homogeneous. Away from such regions, the tensor field approximation does not introduce bias in useful DT-MRI parameters, such as $\text{Trace}(\mathbf{D}(\mathbf{x}))$. It also facilitates the calculation of several new parameters, particularly differential quantities obtained from the tensor of spatial gradients of $\mathbf{D}(\mathbf{x})$. As an example, we show that they can identify tissue boundaries across which diffusion properties change rapidly using *in vivo* human brain data. One important application of this methodology is to improve the reliability and robustness of DT-MRI fiber tractography. © 2002 Elsevier Science

Key Words: MRI; MR; diffusion; DTI; DT-MRI; *in vivo*; tensor; field; interpolation; anisotropy; fiber; tractography; curvature.

INTRODUCTION

Diffusion tensor MRI (DT-MRI) provides a measurement of an effective diffusion tensor of water, \mathbf{D} , in each voxel within an imaging volume (I). However, these diffusion measurements are inherently discrete, noisy, and voxel-averaged. In this work, we view the DT-MRI data as discrete noisy samples of an underlying macroscopic diffusion tensor field, $\mathbf{D}(\mathbf{x})$, where $\mathbf{x} = (x, y, z)$ are the spatial coordinates in the laboratory frame of reference. This field is presumed to be continuous and smooth at a gross anatomical (voxel) length scale within many soft fibrous

tissue regions, including white matter, muscles, ligaments, and tendons.

The main objective in this paper is to develop and describe a mathematical framework to estimate the continuous tensor field, $\mathbf{D}(\mathbf{x})$, from a discrete set of noisy DT-MRI measurements. A continuous model is essential for many important new applications of DT-MRI data in biology and medicine. One application is to improve statistical estimates of histological and physiological MRI parameters, including $\text{Trace}(\mathbf{D}(\mathbf{x}))$, the eigenvalues (principal diffusivities) of $\mathbf{D}(\mathbf{x})$, and measures of diffusion anisotropy (I), similarity, and fiber organization (2, 3). The reliability of these estimates should improve, and bias in their means and variances (4) should be reduced when the approximated diffusion tensor field is used rather than the noisy tensor measurements themselves.

Having a continuous model enables us to compute and display intrinsic² architectural or microstructural MRI parameters based upon tissue fiber geometry (2, 3). Some previously suggested tissue characteristics include the degree of fiber twisting, bending, and diverging (5). New parameters are also presented here to describe architectural features of the tensor field itself, such as how its principal coordinate axes meander within the imaging volume. None of these quantities could be reliably estimated directly from the measured diffusion tensor data, since their evaluation requires spatial differentiation of noisy tensor quantities, which would only further amplify the noise. Below, we show that these parameters can be calculated more reliably and robustly using the smoothed representation of $\mathbf{D}(\mathbf{x})$.

Another important application of this new methodology is to DT-MRI fiber tractography. Here, fiber tract trajectories are represented as streamlines obtained by integrating the fiber direction (vector) field (6, 7). However, integrating a noisy direction vector field can cause these computed fiber trajectories to wander off course (7). Using a smooth representation of the direction field, obtained from the continuous representation

² By an intrinsic parameter, we mean a computed quantity that depicts a characteristic or feature of the tissue, which is independent of the details of the measurement, for instance, of the orientation of the fiber within the magnet, the specifics of the diffusion weighted imaging (DWI) sequences used to estimate the direction, . . . e.g., see (2, 3).

¹ To whom correspondence should be addressed at National Institute of Health, Building 13, Room 3W16, 13 South Drive, Bethesda, MD 20892-5772. E-mail: pjbasser@helix.nih.gov.

of $\mathbf{D}(\mathbf{x})$, however, can improve the fidelity of tract-following schemes (7). Establishing connectivity of neural pathways (i.e., establishing continuous links between different regions of the brain) and continuity (i.e., assessing any disjunction between them) can also benefit from this development.

Moreover, our method provides a unified image-processing framework for performing several generic tasks rapidly and efficiently on DT-MRI and other tensor field data. These tasks include filtering noise, sharpening edges, and detecting boundaries; compressing, storing, and transmitting large image files; interpolating and extrapolating tensor data; resampling data at different resolutions; extracting textural features, segmenting images, clustering tensor data, and classifying tissues; and detecting statistical outliers.

Finally, to our knowledge, this is the first demonstration of a mathematical method that produces a continuous approximation of a discrete, sampled 2nd-order tensor field. While this work has applications to DT-MRI, it has a much broader significance in other areas of natural sciences (e.g., oceanography, meteorology, and materials sciences).

Thus, this paper addresses several critical unmet needs in the analysis and representation of measured DT-MRI data. Here we (a) describe this general mathematical framework that continuously approximates discretely sampled DT-MRI data, (b) test its fidelity, (c) present several exemplary intrinsic MR parameters for tissue structure and architecture that can be calculated using the framework, and (d) apply these parameters to *in vivo* DT-MRI data.

THEORY

Continuous Approximation and Representation of a Discrete Tensor Field

The rigorous theoretical underpinnings of this methodology are provided elsewhere (8), wherein theorems are proved that lay the foundation for the development of a continuous tensor field representation of discrete, noisy diffusion tensor data. Below, we describe the essential features of this methodology. The implementation of this tensor field representation method to measured DT-MRI data is described in the Appendix.

To construct a continuous approximation to a diffusion tensor field, we start with a set of continuous basis functions (approximants) whose linear combinations define an approximation space. This space should possess the following properties to make the approximation scheme practicable:

1. This set of basis functions is sufficiently rich to represent the diffusion tensor field precisely and accurately.
2. The mathematical description of the approximation space is computationally tractable.
3. The approximation of the diffusion tensor field is implemented using algorithms that are fast, robust, and accurate.

To meet these requirements, we use atomic spaces (9), which

are a generalization of shift invariant spaces.³ In particular, we choose an atomic space, $S_{\Delta}(\mathbf{x}, \mathbf{B})$, such that any function in that space, $T_{\Delta}(\mathbf{x})$, is of the form

$$T_{\Delta}(\mathbf{x}) = \sum_{i=1}^r \sum_k \sum_l \sum_m c_i(k, l, m) \times \mathbf{B}^i(x\Delta_x - k, y\Delta_y - l, z\Delta_z - m). \quad [1]$$

Each approximant, $T_{\Delta}(\mathbf{x})$, in the approximation space, $S_{\Delta}(\mathbf{x}, \mathbf{B})$, is a weighted sum of a finite number of tensor field generators, $\mathbf{B}^i(\mathbf{x}, \Delta) | \{i = 1, \dots, r\}$, and their shifts are on a uniform grid within the imaging volume, as indicated by k , l , and m . In our DT-MRI application, the dimensionality of the tensor field r equals 6 (which is the number of independent elements of the symmetric 2nd-order diffusion tensor). The coefficients, c_i , are the unknown parameters in the continuous model. The scale parameters, Δ_x , Δ_y , and Δ_z , control the degree of smoothness of this representation in each direction.

When all scale parameters equal 1, the continuous representation becomes interpolation; i.e., the continuous tensor field passes through each of the discrete tensor data precisely. When one or more of the Δ_i is less than 1, the continuous representation becomes a data reduction technique that approximates or “fits” the discrete tensor data. Additionally, when one or more of the Δ_i are greater than 1, the continuous representation becomes a data expansion technique that oversamples the discrete tensor data. In our DT-MRI measurements, the resolution along the z axis (slice-select direction) is approximately half that along x and y . To obtain an isotropic grid of B -spline coefficients one could oversample the data along the z direction by setting $\Delta_z = V_r \Delta_x = V_r \Delta_y$, where V_r is the voxel aspect ratio ($V_r \cong 2$ in our case). However, in practice it can be beneficial to impose the constraint $0 < \Delta_i \leq 1$, to preserve the measured signal values at the measurement points.

The optimal choice of the coefficients, c_i , for a given choice of tensor field generators and scale parameters is the one that minimizes the least-squared difference between the original tensor data and the approximated diffusion tensor field (8).

We showed previously that finding the tensor field generator can be reduced to finding a continuous representation of each of its individual tensor components (8). In particular, to represent the field of the symmetric diffusion tensor, we proposed the following six tensor field generators used in Eq. [1] to define the tensor approximation space, $S_{\Delta}(\mathbf{x}, \mathbf{B})$:

$$\mathbf{B}^1(\mathbf{x}) = b^1(\mathbf{x}) \begin{bmatrix} 1 & 0 & 0 \\ 0 & 0 & 0 \\ 0 & 0 & 0 \end{bmatrix}, \quad \mathbf{B}^2(\mathbf{x}) = b^2(\mathbf{x}) \begin{bmatrix} 0 & 0 & 0 \\ 0 & 1 & 0 \\ 0 & 0 & 0 \end{bmatrix}$$

³ Atomic spaces are used in solving differential equations by finite element methods and in wavelet theory.

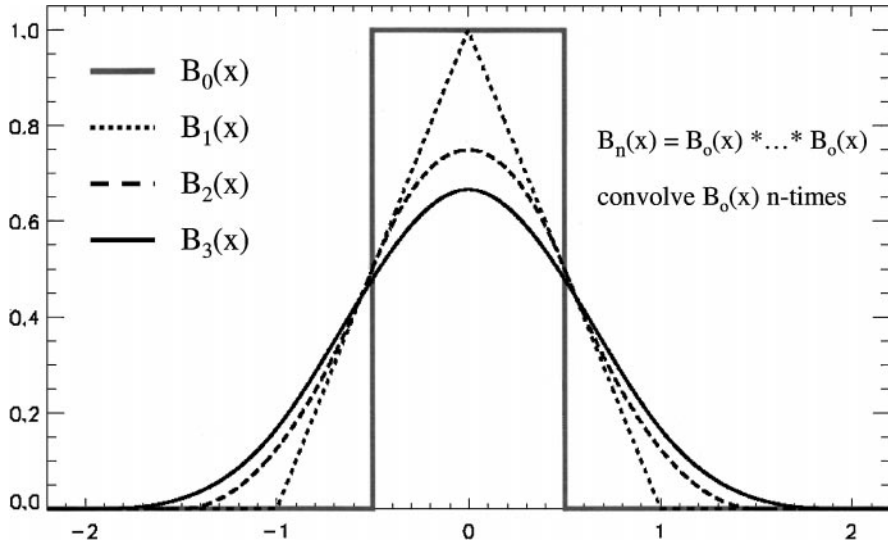


FIG. 1. A graph of the 1-D B-spline functions of order 0 through 3. The B-spline of order n is obtained by repeating n times the convolutions of the box function (the B-spline of order 0) as indicated in the figure.

$$\begin{aligned} \underline{B}^3(\mathbf{x}) = b^3(\mathbf{x}) & \begin{bmatrix} 0 & 0 & 0 \\ 0 & 0 & 0 \\ 0 & 0 & 1 \end{bmatrix}, & \underline{B}^4(\mathbf{x}) = b^4(\mathbf{x}) & \begin{bmatrix} 0 & 1 & 0 \\ 1 & 0 & 0 \\ 0 & 0 & 0 \end{bmatrix} & [2] \\ \underline{B}^5(\mathbf{x}) = b^5(\mathbf{x}) & \begin{bmatrix} 0 & 0 & 1 \\ 0 & 0 & 0 \\ 1 & 0 & 0 \end{bmatrix}, & \underline{B}^6(\mathbf{x}) = b^6(\mathbf{x}) & \begin{bmatrix} 0 & 0 & 0 \\ 0 & 0 & 1 \\ 0 & 1 & 0 \end{bmatrix}. \end{aligned}$$

Thus, each tensor field generator, $\underline{B}^i(\mathbf{x})$, can be expressed in terms of a single function, $b^i(\mathbf{x})$, which now serves as a basis for the i th component of the tensor field. Furthermore, these $b^i(\mathbf{x})$ are themselves chosen to be a product of one-dimensional functions, i.e., $b^i(\mathbf{x}) = f^i(x)g^i(y)h^i(z)$. The basis functions are now separable in two ways, first with respect to the components of the tensor, and second with respect to x , y , and z . Thus, the task of finding a continuous tensor field, $\underline{D}(\mathbf{x})$, or more precisely the coefficients of the continuous model, c_i , is reduced to applying a one-dimensional signal approximation algorithm sequentially along x , y , and z coordinates within the imaging volume for each tensor component. This one-dimensional approximation algorithm is described in more detail in the Appendix. In our implementation, we choose $f^i(x)$, $g^i(y)$, and $h^i(z)$ to be the B-spline functions, which are obtained by repeated convolutions of the simple box function (Fig. 1). The number of convolutions determines the order of the B-spline, i.e., linear, quadratic, cubic, etc. The use of the separable basis function provides an easy way to account for the nonuniform resolutions in x , y , and z directions in a typical DT-MRI experiment, where resolution is typically higher “in-plane” than along the slice-select direction.

As Fig. 2 demonstrates, the two-dimensional spline function constructed using a product of linear one-dimensional B-splines is anisotropic (i.e., shows preferential directions) and will pro-

duce artifacts when used for scaling (i.e., smoothing) a general tensor field. However, when the cubic B-splines are used these artifacts are negligibly small and the $b^i(\mathbf{x})$ constructed in this way perform nearly as well as the true two-dimensional isotropic basis functions (Fig. 2), but are much more computationally efficient to implement. In our implementation we use mainly the cubic B-splines. If higher order derivatives are needed, it is advisable to use B-splines of higher polynomial order than three to preserve the isotropic properties of the multidimensional basis functions.

B-spline functions have several other important advantages which make this implementation highly efficient: (1) the generators have finite spatial extent (i.e., finite support), which speeds up and simplifies digital processing algorithms; (2) the tensor field generators can be expressed analytically, thus the tensor field can be evaluated exactly at any point within the imaging volume; (3) one can control the degree of smoothness and

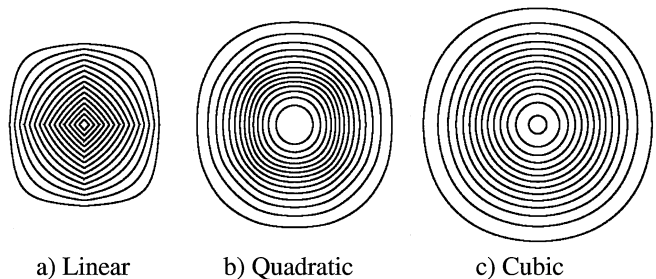


FIG. 2. The contour plot of the two-dimensional B-spline functions constructed using the assumption of separability. One can see that the separability assumption does not hold well for the B-splines of order 2 and below (linear and quadratic) while for the cubic B-splines the two-dimensional version does not show any significant difference from the true isotropic two-dimensional splines.

TABLE I
Forms of the Tensor Field, $\mathbf{D}(\mathbf{x})$, Which Can be Used to Describe Diffusion Properties of Different Media

Tensor fields, $\mathbf{D}(\mathbf{x})$	Homogeneous	Heterogeneous
Isotropic	$\langle \mathbf{D} \rangle \mathbf{I}$	$\langle \mathbf{D}(\mathbf{x}) \rangle \mathbf{I}$
Anisotropic	$\mathbf{R}^T \underline{\Delta} \mathbf{R}$	$\mathbf{R}(\mathbf{x})^T \underline{\Delta}(\mathbf{x}) \mathbf{R}(\mathbf{x})$

Note. In the isotropic case, $\langle \mathbf{D} \rangle$ is the orientationally averaged (scalar) mean diffusivity, and \mathbf{I} is the identity tensor. In the anisotropic case, \mathbf{R} is a proper rotation matrix and $\underline{\Delta}$ is the matrix of eigenvalues. $\langle \mathbf{D}(\mathbf{x}) \rangle$, $\mathbf{R}(\mathbf{x})$ and $\underline{\Delta}(\mathbf{x})$ are assumed to be piecewise continuous functions of x , y , and z within the imaging volume.

differentiability of the continuous approximation by changing the polynomial order or degree of the B-spline functions; (4) by adjusting the scale parameters (Δ) of the B-spline representation we can choose among oversampling ($\Delta > 1$), interpolation ($\Delta = 1$, i.e., fitting data points exactly), and approximation ($\Delta < 1$, i.e., fitting data points approximately); (5) the derivatives of B-splines can be expressed recursively in terms of the original B-splines; and (6) B-spline functions naturally generate multiresolution structures that are useful in analyzing signals and images at different length scales.

Statistical Properties of the Approximated Tensor Field

It is important to keep in mind that the continuous tensor field is still a statistical estimate of the “true” underlying tensor field. Elsewhere, we showed that the elements of the diffusion tensor obtained by DT-MRI are distributed according to a multivariate Gaussian probability density function (I_0) in which \mathbf{D} is expressed as a six-dimensional vector, $\tilde{\mathbf{D}} = (D_{xx}, D_{yy}, D_{zz}, D_{xy}, D_{xz}, D_{yz})^T$, whose distribution can be written as

$$p(\tilde{\mathbf{D}}) = \frac{1}{\sqrt{(2\pi)^6 |\Sigma|}} \exp\left(-\frac{1}{2}(\tilde{\mathbf{D}} - \mathbf{M})^T \Sigma^{-1}(\tilde{\mathbf{D}} - \mathbf{M})\right), \quad [3]$$

where $\mathbf{M} = (\mu_{xx}, \mu_{yy}, \mu_{zz}, \mu_{xy}, \mu_{xz}, \mu_{yz})^T$ is the six-dimensional mean vector, and Σ is the 6×6 -covariance matrix.

Since the approximate tensor field is always a linear function of these measured tensors, the coefficients, c_i , of the continuous model will also be normally distributed. Moreover, the mean-squared error between the noisy discrete data sampled within the imaging volume and the continuous field representation will be χ^2 distributed.

The approximated tensor field elements will have a lower variance than the original measured tensor data. The factor by which the variance of the noise is reduced using our approximation method scales as $\Delta_x \Delta_y \Delta_z$. The “exact”⁴ expression for the variance of c_i can be obtained using the linear relationship

⁴ Strictly speaking, this is not an exact relationship because one of the filters in Eq. [A.2] is an infinite impulse response (IIR).

between the measured data and the coefficients (see Eqs. [A.2] and [A.6]). This relationship can be simplified in the case of the homogeneous field (see Table 1). In the case of the heterogeneous diffusion tensor field, evaluating the noise properties is more complex, partly due to the fact that the variance of the original diffusion tensor elements is not homogeneous.

METHODS

Implementation of Algorithms for Tensor Field Approximation

The first step in the implementation is to choose the appropriate order of the B-spline functions to generate the basis of the diffusion tensor field and the appropriate scale parameters, Δ_j . Specifically, Δ_j is the ratio of the number of unknown parameters to the number of measured data points for the 1-D approximation in the j th direction. This means that the scale parameters can only take on specific rational values, $\{\Delta\}_N$, which designates the rational number closest to Δ that contains N in the denominator. For DT-MR images, N is usually large enough to allow sufficient precision in the range of the scale parameter values between 0 and 1. We further reduce the number of scale parameters by choosing only one Δ and by assigning the three values of the model as $\Delta_x = \{\Delta\}_{N_x}$, $\Delta_y = \{\Delta\}_{N_y}$, $\Delta_z = \{V_r \Delta\}_{N_z}$, where V_r is the voxel aspect ratio as described earlier and with the constraint that $\Delta \in [0, 1]$. The choice of rational scales allows us to use the same transformation for the reduction and expansion operations and ensures that the doubly transformed (contracted and expanded back) discrete signals are sampled at exactly the same points in the space. Ideally, the value of Δ should be twice the ratio of the maximal spatial frequency of the “pure” (noise-free) signal and the sampling frequency. Note, however, that our approximation method is not a simple low-pass filter. In cases where structures within the image appear at all length scales, the choice of Δ is empirical as the structures on the small scales (single or a few voxels) must be blurred in order to improve estimates of large structures of the diffusion tensor field elsewhere.

Once the B-spline order and the scale parameters are chosen for a given DT-MRI data set, the second step is to calculate B-spline coefficients in the x , y , and z directions for each of the six independent diffusion tensor elements using the spatial separability property described above. Thus, we perform 1-D transforms repeatedly on the tensor data set using methods reported in (11–14), some of which are also summarized in the Appendix.

Moreover, the same tensor representation algorithms can be used for interpolating or approximating the tensor data. Interpolation forces the smoothed representation to pass through each measured tensor datum exactly, while approximation entails obtaining a smoothed representation of lower spatial resolution that passes through the data points only approximately. The difference between these two schemes is illustrated in Fig. 3 where

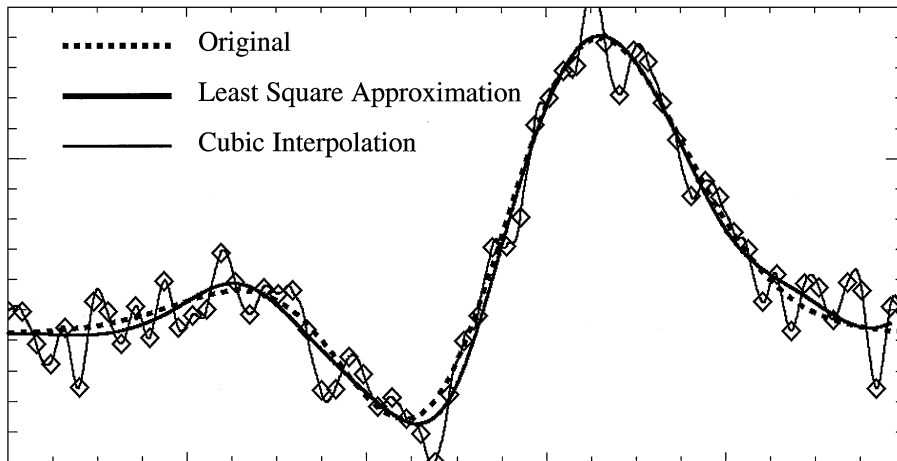


FIG. 3. Illustration of the difference between interpolating and approximating one-dimensional data using B-spline functions. While the interpolation function fits the noisy data exactly, the approximation function fits the noisy data only approximately, in a least-square sense. The diamonds represent the noisy signal. The dotted line represents the original synthesized continuous curve which was sampled and to which 10% (relative to the peak) Gaussian noise was added. The thick solid line is the B-spline least-squares approximation using the scaling factor $\Delta = 0.25$, while the thin solid line is obtained using the standard cubic interpolation of the same data.

the thick solid line is the B-spline least squares approximation to the noisy data (diamonds) using the scaling factor $\Delta = 0.25$. The thin solid lines represent the cubic B-spline interpolation to the same data using the scaling factor $\Delta = 1$. They are compared to the “true” curve (dotted line). Only the approximated curve furnishes a reasonable estimate of the first derivative.

Synthetic Diffusion Tensor Fields to Test the Tensor Field Approximation

We have also synthesized a family of continuous diffusion tensor fields that represent structural or architectural motifs within a tensor field. These “templates” or simulated phantoms are used primarily to test the fidelity of the tensor approximation and to help identify unexpected pathologies or anomalies that may arise in its implementation. In the most general case, these templates are constructed by writing $\mathbf{D}(\mathbf{x})$ in terms of its three Euler angles, $\phi(\mathbf{x})$, $\theta(\mathbf{x})$, and $\psi(\mathbf{x})$, which appear in the rotation matrix, $\mathbf{R}(\mathbf{x})$, and its three eigenvalues, $\lambda_1(\mathbf{x})$, $\lambda_2(\mathbf{x})$, and $\lambda_3(\mathbf{x})$, which appear as diagonal elements of $\mathbf{\Lambda}(\mathbf{x})$ (15),

$$\mathbf{D}(\mathbf{x}) = \mathbf{R}(\mathbf{x})^T \mathbf{\Lambda}(\mathbf{x}) \mathbf{R}(\mathbf{x}). \quad [4]$$

Devising a tensor field with particular geometric or architectural features is reduced to specifying these six scalar quantities above as functions of \mathbf{x} . Equation [4] is used for the most general case of a heterogeneous, anisotropic tensor field; however, simpler expressions than Eq. [4] are used for the homogeneous isotropic, homogeneous anisotropic, and heterogeneous isotropic cases. These are given in Table 1.

Using piecewise continuous functions for the six scalar functions, we can readily construct heterogeneous tensor fields whose fiber patterns have distinct anatomical correlates such

as fiber crossing, kissing, merging, branching, circulating, diverging, converging, kinking, terminating, etc. Tensor fields are also constructed to represent fiber sheets that twist or bend. We can also introduce geometric singularities in the tensor field, such as sources or sinks of fibers (5, 15).

Testing Noise Immunity

Monte Carlo simulations of DT-MRI experiments were performed to test noise immunity of the tensor approximation scheme. This is done by sampling the continuous analytical diffusion tensor templates in each voxel, and then adding Ricean background noise to the ideal NMR signal (16) as described previously (4). In this way noisy realizations of the tensor field templates can be generated with known noise characteristics.

Testing the Robustness and Fidelity of the Continuous Approximation

One method to report the fidelity of the tensor field approximation is to calculate the percentage error between the tensor field template and the approximated tensor field, which we define as

$$\begin{aligned} \% \text{Error}(\mathbf{x}) &= 100 * \frac{|\mathbf{D}(\mathbf{x}) - \bar{\mathbf{D}}(\mathbf{x})|}{|\mathbf{D}(\mathbf{x})|} \\ &= 100 * \sqrt{\frac{\sum_{i=1}^3 \sum_{j=1}^3 (D_{ij}(\mathbf{x}) - \bar{D}_{ij}(\mathbf{x}))^2}{\sum_{i=1}^3 \sum_{j=1}^3 (D_{ij}(\mathbf{x}))^2}}, \quad [5] \end{aligned}$$

where $\mathbf{D}(\mathbf{x})$ is the original analytic tensor field, and $\bar{\mathbf{D}}(\mathbf{x})$ is the approximated tensor field. The quantity above measures, in a root-mean-squared sense, the fractional error between the two fields at each point within the imaging volume. We use this

quantity as a measure of the goodness-of-fit of our B-spline approximation model to the data, similar to χ^2 .

DT-MRI Methods

Healthy volunteers were scanned using a 1.5-T GE Signa Horizon EchoSpeed equipped with a 2.2-G/cm gradient set, using an approved NIH clinical protocol. A set of diffusion-weighted images (DWIs) was acquired with diffusion gradients applied in six isotropically distributed directions using an interleaved, spin-echo, echo-planar sequence, employing navigator echo correction (see (17)). DWI parameters were FOV = 22 cm, TE = 78 ms, TR > 5 s with cardiac gating, voxel size = $3.5 \times 1.75 \times 1.75$ mm, data matrix = 128×128 . The degree of diffusion weighting, as measured by Trace(\mathbf{b}) (where \mathbf{b} is the b-matrix (18–20) calculated for each DWI) is varied from approximately 0 to 1000 s/mm². An effective diffusion tensor was calculated in each voxel according to (18). Maps of useful DT-MRI parameters were calculated from the diffusion tensor, such as Trace(\mathbf{D}), and diffusion anisotropy measures such as the lattice index (4).

Parameters Derived Using the Continuous Approximation

The DT-MRI parameters presented below, which are calculated from the continuous approximation of the diffusion tensor field, characterize distinct, intrinsic structural or architectural features of the tissue. We choose to represent quantities that require spatial differentiation of components of the tensor field or of the fiber direction field. We expect our methodology to have a particular advantage in evaluating such quantities, since spatial differentiation of noisy quantities only amplifies noise (e.g., see (21)). By first obtaining an approximate, sufficiently smooth continuous representation of the diffusion tensor and of its direction field, we can obtain smooth continuous representations of spatial derivatives of these quantities as well. Since our method approximates the tensor field data with B-spline tensor fields, we can even obtain analytical expressions for these quantities within an imaging volume.

The spatial rate of change of the tensor field, i.e., the “gradient” of the tensor field, is a 3rd-order tensor whose elements are

$$D(\mathbf{x})_{ij,k}, \quad [6]$$

where i and j indicate the tensor component, and k indicates the coordinate direction along which partial derivatives are taken. A new scalar function that we propose here summarizes an intrinsic feature of the tensor field. It is obtained by a scalar contraction (tensor inner product) or $D(\mathbf{x})_{ij,k}$ with itself:

$$\sum_{i=1}^3 \sum_{j=1}^3 \sum_{k=1}^3 D(\mathbf{x})_{ij,k} D(\mathbf{x})_{ij,k}. \quad [7]$$

Just as the square of the magnitude of the gradient, $|\nabla c(\mathbf{x})|^2$, detects changes of spatial intensity of a scalar field, $c(\mathbf{x})$, Eq. [7] detects changes in “intensity” of a 2nd-order tensor field. Because Eq. [7] is a scalar contraction of two 3rd-order tensors, it is inherently a rotationally invariant quantity, so that its value is unchanged when the laboratory coordinate system or the sample is rotated.

It is also useful to decompose the total diffusion tensor field into its isotropic and deviatoric parts (see (2)) at each point, \mathbf{x} , within the imaging volume:

$$\mathbf{D}(\mathbf{x}) = \underbrace{\langle \mathbf{D}(\mathbf{x}) \rangle}_{\text{isotropic}} \mathbf{I} + \hat{\mathbf{D}}(\mathbf{x}) \quad [8]$$

Above, $\langle \mathbf{D}(\mathbf{x}) \rangle = (D_{xx}(\mathbf{x}) + D_{yy}(\mathbf{x}) + D_{zz}(\mathbf{x}))/3$ is the scalar orientationally averaged mean diffusivity at a particular point, $\hat{\mathbf{D}}(\mathbf{x})$ is the deviation tensor there, and \mathbf{I} is the identity tensor. When the gradient and contraction operators are applied individually to the isotropic and anisotropic parts of $\mathbf{D}(\mathbf{x})$, we obtain

$$3 \left(\left(\frac{\partial \langle \mathbf{D}(\mathbf{x}) \rangle}{\partial x} \right)^2 + \left(\frac{\partial \langle \mathbf{D}(\mathbf{x}) \rangle}{\partial y} \right)^2 + \left(\frac{\partial \langle \mathbf{D}(\mathbf{x}) \rangle}{\partial z} \right)^2 \right) \quad [9a]$$

and

$$\sum_{i=1}^3 \sum_{j=1}^3 \sum_{k=1}^3 \left(\frac{\partial \hat{D}_{ij}(\mathbf{x})}{\partial x_k} \right)^2, \quad [9b]$$

respectively. Equation [9a] is the sum of squares of the x , y , and z components of the gradient of the orientationally averaged or mean diffusivity; Eq. [9b] is the sum of squares of the x , y , and z components of the gradient of each component of the deviation tensor.

Other tensor-derived parameters characterize features of the curving and twisting of the triad of eigenvectors within the imaging volume, or equivalently, of the three level surfaces that lie perpendicular to each of the three eigenvectors of $\mathbf{D}(\mathbf{x})$, at any point. While calculating these quantities is arduous using Christoffel symbols (e.g., see (22)), we propose a simpler means to calculate at least one type of curvature measure below.

The curvature of a fiber tract within the imaging volume can be obtained from the fiber tract trajectory, described by $\mathbf{r}(s)$, and its local tangent vector, $\mathbf{t}(s)$. The local curvature, $\kappa(s)$, is given by

$$\kappa(s) = \left| \frac{d\mathbf{t}(s)}{ds} \right| = \left| \frac{d \left(\frac{\mathbf{r}'(s)}{|\mathbf{r}'(s)|} \right)}{ds} \right|, \quad [10]$$

which can be plotted as a function of s along a tract. Calculation of Eq. [10] can be performed either locally at point \mathbf{x} by expressing s as a function of x , y and z , $s(x, y, z)$, and numerically

evaluating its infinitesimal neighborhood in the continuous tensor field. Another method is to construct a 3-D space curve $\mathbf{r}(s)$, a mathematical fiber tract, as in (7). The latter allows us to impose additional and much stronger smoothness constraints, by scaling the s space to yield more reliable estimates of $\kappa(s)$.

RESULTS

Figure 4 illustrates the improvements in the fiber field direction map that results from using the approximated tensor field. Noise is added to a tensor field template of a straight nerve fiber (SNR = 15). Figure 4a shows the unapproximated fiber direction field data, while Fig. 4b shows the results obtained when using the approximated tensor data.

Figure 5 illustrates the empirical statistical distribution of $\text{Trace}(\mathbf{D}(\mathbf{x}))$ in a region of interest (ROI) of a simulated phantom having uniform diffusion properties. These distributions are plotted against the coarseness of the smoothing window for an SNR of 15. As the smoothing window size increases, the distribution becomes sharper, but no bias is introduced in the mean, nor is the distribution skewed by the approximation. In fact, the known Gaussian distribution of $\text{Trace}(\mathbf{D}(\mathbf{x}))$ (10) is preserved using this approximation scheme, demonstrating that its application does not change the underlying statistical distribution.

Figure 6 illustrates two tensor field templates, one representing two fiber bundles crossing (Fig. 6a) and one a fiber forming a ring (Fig. 6b). Values used in constructing these templates are typical of those observed *in vivo* (23) (i.e., for parenchyma $\text{Trace}(\mathbf{D}) = 2100 \mu\text{m}^2/\text{s}$, for cerebrospinal fluid (CSF) $\text{Trace}(\mathbf{D}) = 10,000 \mu\text{m}^2/\text{s}$, and for white matter, the anisotropy ratio is in the range $A_r \in [2, 10]$). In Fig. 6, the anisotropy ratio in the simulated phantoms was $A_r = 3$ ($\lambda_1/\lambda_3 = 3$ and $\lambda_2 = \lambda_3$). The phantoms are constructed using Eq. [4]. For the ring phantom we specify that a voxel contains the white matter fiber if $r_1 < r = \sqrt{(x - x_c)^2 + (y - y_c)^2} < r_2$, where

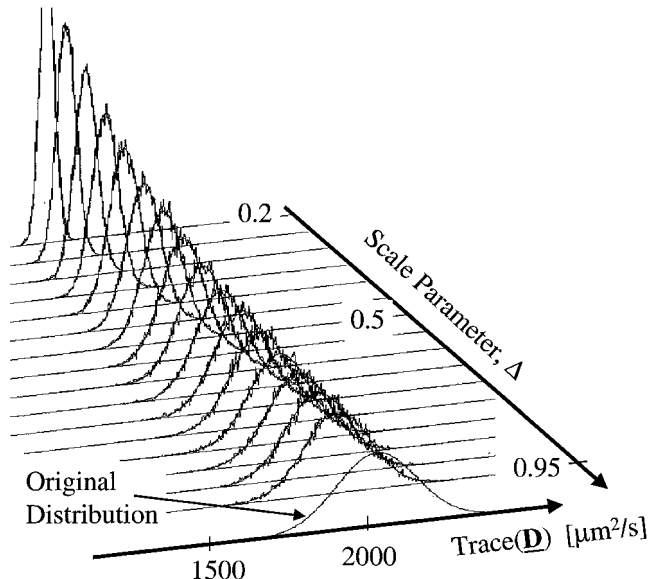


FIG. 5. Illustration of an empirical statistical distribution of $\text{Trace}(\mathbf{D}(\mathbf{x}))$ in an ROI of a simulated phantom of a tissue having uniform diffusion properties and with simulated SNR = 15. These distributions are plotted against the scale parameter Δ . Decreasing Δ (i.e., increasing the smoothing window) reduces the variance of the distribution without introducing a bias in the mean. Moreover, no skewness is introduced into the distribution by the approximation method. Empirical histograms of approximated data are plotted together with the corresponding fit to Gaussian distribution. The Gaussian plotted on the line corresponding to $\Delta = 1$ represents the statistical distribution of the original data. All data are well approximated by the normal distribution. Gaussian distributions fit to each of the histograms show that applying this approximation scheme preserves the underlying distribution of $\text{Trace}(\mathbf{D}(\mathbf{x}))$.

r_1 and r_2 are the inner and outer radii and x_c and y_c are the coordinates of the center of the ring. For such voxels we set $\lambda_1 = 3\lambda_2 = 3\lambda_3 = 1260 \mu\text{m}^2/\text{s}$ and choose the Euler angle, $\phi(\mathbf{x})$, so that the eigenvector associated with the largest

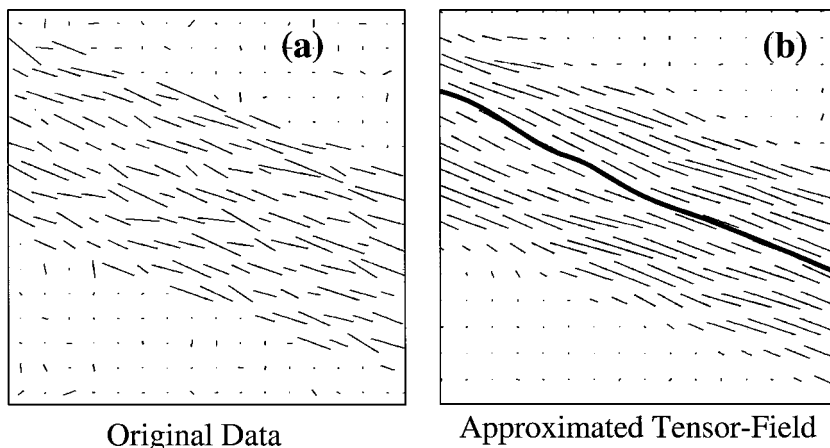


FIG. 4. Illustration of how using the approximated tensor field improves the reliability of fiber tractography. Here, noise is added to a tensor field template of a straight nerve fiber (SNR = 15). Line segments depict the principal axis of the largest principal diffusivity of the diffusion tensor at each sampled point. (a) The computed discrete direction field obtained from the raw diffusion tensor data; (b) the fiber direction field and a fiber tract computed from the approximated tensor data.

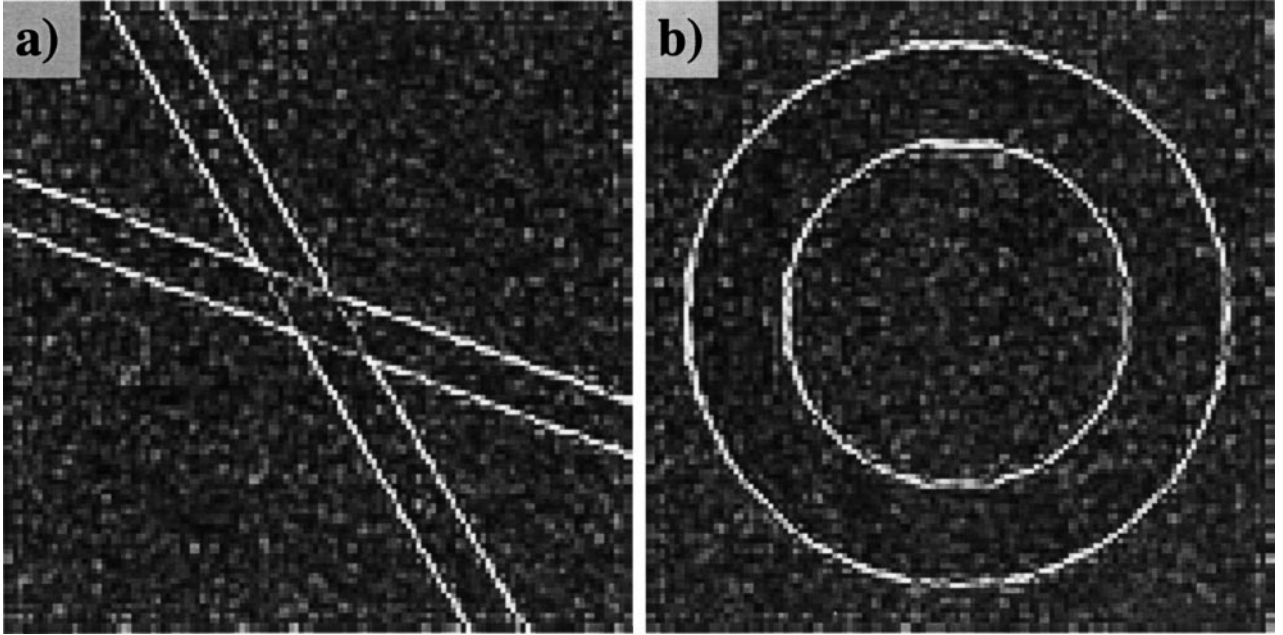


FIG. 6. The calculated percent error, according to Eq. [5]. The two tensor field templates (a) representing two fiber bundles crossing, and (b) containing two concentric rings were created to which noise ($SNR=25$) was added before performing the approximation. A map of the %-error shows that the fit is good in homogeneous regions within the simulated phantoms, and only deviates at the edges where tissue properties change abruptly. The scale parameter was 0.5. The “white” on this grayscale image represents the 20% or greater error (35% was the maximal error), while “black” represents 0% error.

eigenvalue is always perpendicular to the line connecting the center of the ring (x_c, y_c, z) and a voxel (x, y, z) on the circle. Because of symmetry, the other two Euler rotations are not performed, i.e., $\theta(\mathbf{x}) = 0$, and $\psi(\mathbf{x}) = 0$. The remaining voxels are assigned properties of gray matter, for which the Euler angles are irrelevant since all eigenvalues are equal: $\lambda_1 = \lambda_2 = \lambda_3 = 700 \mu\text{m}^2/\text{s}$. Both these simulated phantoms are quasi-three-dimensional in that they span more than one slice; however, there is no variability along the z dimension. To these diffusion tensor phantoms we also add Ricean noise as described under Methods (*Testing Noise Immunity*). We use these templates to assess the quality of the fit of the diffusion tensor field, as measured using Eq. [5]. A map of the %-error is plotted, showing that the fit is good in homogeneous regions within the simulated phantoms and only deviates significantly at the margins where tissue properties change abruptly.

Figure 7a shows an anisotropy index of a diffusion tensor template in which circumferentially wound fiber bundles are organized in concentric rings. Figure 7b shows the radius of curvature computed locally from the approximated tensor field using Eq. [10]. The radius of curvature ranges from dark (small) to bright (large), as we move from the inner to the outer rings. The intra-ring variation in intensity is due to noise added to the phantom, which introduces large fluctuations in the calculated curvature. The estimates of the curvature in Fig. 7b are so noisy even with a smooth representation ($\Delta = 0.5$) because the calculation of curvature involves higher (second) derivatives of the noisy vector field $\varepsilon_1(\mathbf{x})$, which is the field of the eigenvector as-

sociated with the largest eigenvalue. This noise is significantly greater when only interpolation is used to calculate the curvature. A more robust way to estimate the curvature of $\varepsilon_1(\mathbf{x})$ is to track its streamline and then estimate the curvature of the resulting space curve, as described under Methods. The radius of curvature estimated in this way is much more accurate and stable as is demonstrated in Fig. 7c.

Figure 8a illustrates a tensor field template representing a highly simplified corpus callosum near a ventricle. A semicircular ring is constructed with anisotropic diffusion properties of brain white matter having its principal fiber directions oriented circumferentially. Above the ring lies a cylindrical region containing an isotropic medium with the same diffusion properties as CSF. The remainder of the imaging volume is filled with an isotropic medium having the same diffusion properties as gray matter. Values used in constructing this template are taken from (23). Figures 8b, 8c, and 8d respectively show results of applying the functions given in Eqs. [7], [9a], and [9b] to the simulated phantom shown in Fig. 8a. Figure 8b shows the result of taking the tensor inner product of the gradient of the anisotropic part of the diffusion tensor with itself. This image distinguishes the margin of the white matter with the CSF and with gray matter. Figure 8c shows the result of taking the tensor inner product of the gradient of the isotropic part of the diffusion tensor with itself. This image distinguishes the margin of the CSF and parenchyma but does not distinguish the boundary of the white matter and gray matter. Figure 8d shows the result of taking the tensor inner product of the gradient of the diffusion tensor with

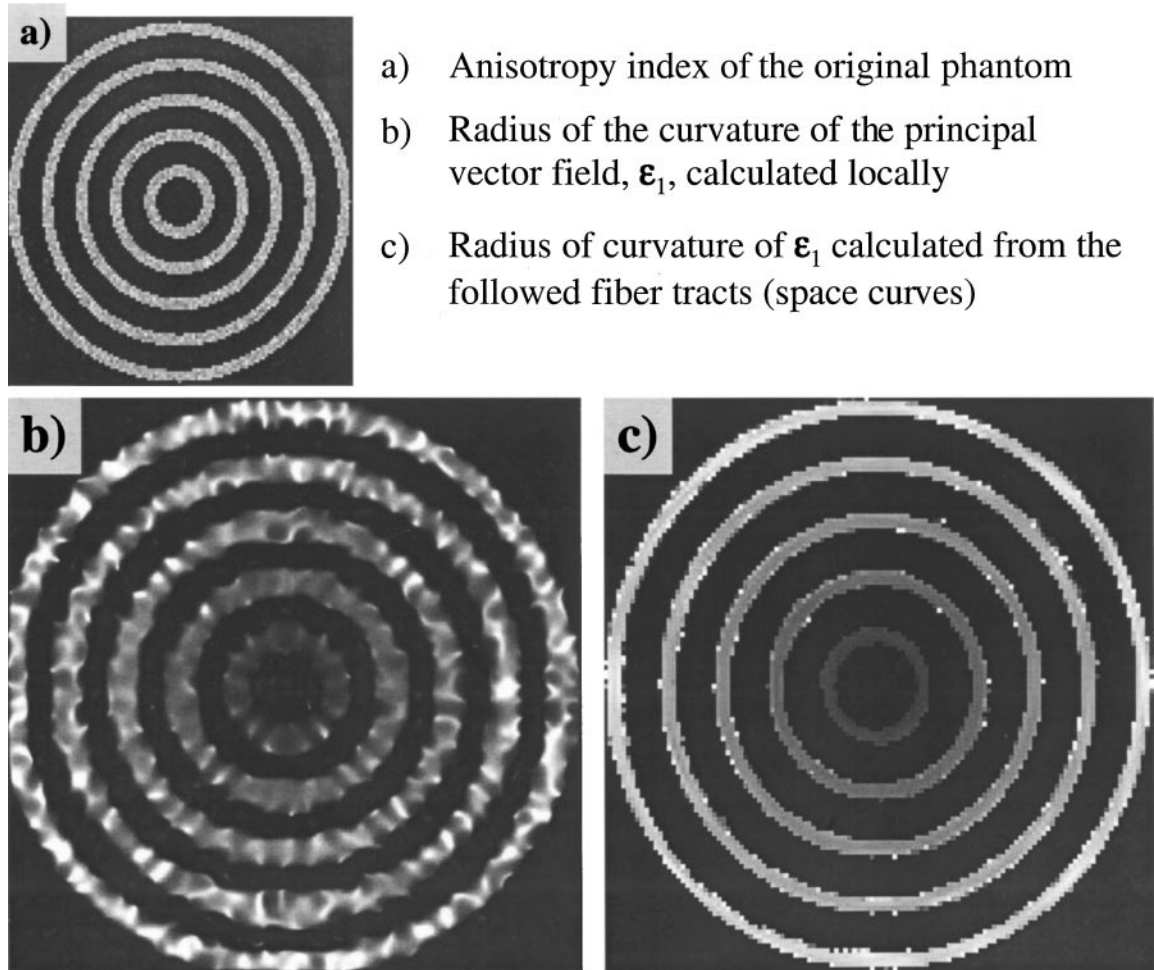


FIG. 7. A diffusion tensor template (a) in which circumferentially wound fiber bundles are organized in concentric rings. A map of the local radius of curvature, computed from the approximated tensor field ($\Delta = 0.5$), is shown in (b). The radius of curvature ranges from dark (small) to bright (large) from the inner to the outer rings. The intra-ring variation in intensity is seen. (c) The curvature obtained by following the field of the eigenvector associated with the largest eigenvalue, $\mathbf{\epsilon}_1(\mathbf{x})$, and then evaluating the curvature of the obtained 3-D space curve using similar approximation methodology (instead of a tensor field it is applied to a 3-D vector-valued 1-D field) with $\Delta = 0.1$. The “white” in the images represents the following values of radius of curvature, (b) 300 voxels and (c) 120 voxels, while “black” represents the radius of 5 voxels in both images. These phantoms are realized on a 128×128 grid in the x - y plane. The white spots in (c) come from the trajectories that have exited into the gray matter region.

itself. This image does not distinguish well between anisotropic and isotropic media, but does show clearly the boundaries between the three distinct regions within the simulated phantom. The “square of the magnitude of the gradient” in Fig. 8b appears to be larger at multiples of 45° than at multiples of 90° . This effect is generally not as pronounced as this figure would suggest, particularly when high-resolution images are simulated (the phantom in Fig. 8 is created on a 64×64 grid). Also, such effects are not observed when our *in vivo* data are processed (Figs. 9 and 10). Although this artifact could be partly due to our use of separable basis functions, we attribute it primarily to the different textures of the discrete boundary (between the CSF and GM) in the 45° and 90° regions of our template, as can be seen in Fig. 8a. In the future we plan to simulate partial volume effects in our templates and expect such asymmetry to

disappear. Additionally, using splines of higher than 3rd order should diminish any contribution the separate basis functions could have to this effect.

Figure 9a shows a $\text{Trace}(\mathbf{D}(\mathbf{x}))$ axial image of a normal subject. Juxtaposed in Fig. 9b is an image of the tensor inner product of the gradient of the isotropic part of the diffusion tensor field. Note that the boundaries between regions in which there are differences in $\text{Trace}(\mathbf{D}(\mathbf{x}))$ —i.e., between CSF and parenchyma in the gyri and sulci, and in the ventricles—are clearly visible, but otherwise, the image is of relatively uniform intensity.

Figure 10a shows a lattice anisotropy index axial image of a normal subject. Juxtaposed in Fig. 10b is the corresponding image of the tensor inner product of the gradient of the anisotropic part of the diffusion tensor field (equivalent to the square of the magnitude of the gradient). Note that the boundaries between

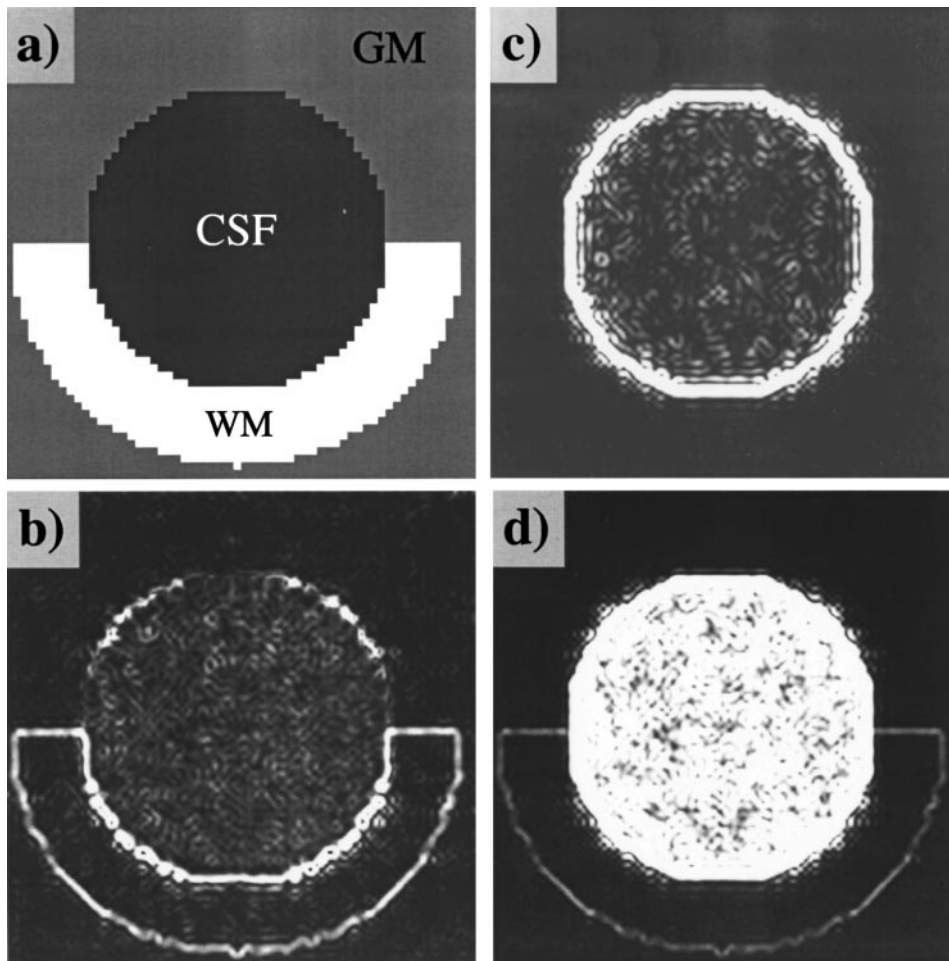


FIG. 8. (a) A simulated phantom of a highly simplified brain region containing the corpus callosum. (b), (c), and (d) Respectively show results of applying the functions given by Eqs. [7], [9a], and [9b] to this phantom. (b) The scalar product of the anisotropic part of the gradient of the diffusion tensor with itself. This image highlights the margins of the white matter (WM) with the cerebrospinal fluid (CSF) and with gray matter (GM). (c) The scalar product of the isotropic part of the gradient of the diffusion tensor with itself. This image distinguishes the margin of the CSF and parenchyma but does not distinguish the boundary of white matter and gray matter. (d) The scalar product of the gradient of the diffusion tensor with itself. This image does not distinguish well between anisotropic and isotropic media, but does show clearly boundaries between the three distinct tissue types within the simulated phantom. The scale parameter used for these figures was 0.8. The “white” in the images represents the following values of the magnitude of the gradient (the square root of what is displayed), (b) $1.5 \mu\text{m}^2/\text{s}/\text{voxel}$, (c) and (d) $1400 \mu\text{m}^2/\text{s}$ voxel, while “black” is equal to 0.

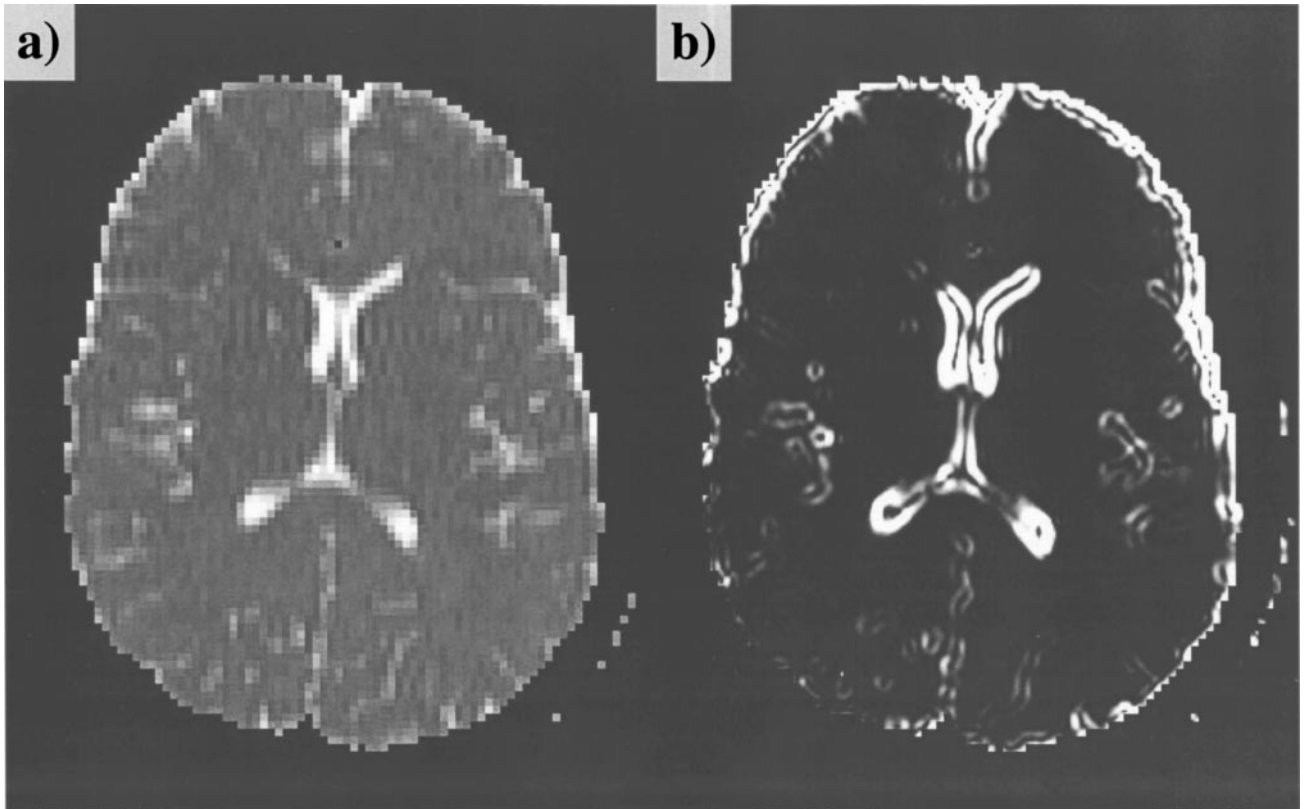
white matter and gray matter are highlighted, but no signal is observed in the CSF or in gray matter *per se*.

DISCUSSION

Having implemented and examined the behavior of the continuous model of diffusion tensor data, we conclude that approximation has many advantages over interpolation. The advantage is particularly evident in estimating quantities that involve spatial differentiation of tensor components or other quantities derived from them. The main limitation of this technique is its smoothness constraint, which tends to blur structures on the order of a single or a few voxels.

It is worth mentioning that our continuous approximation does not ensure that the approximate tensor field is positive definite at

all points \mathbf{x} within the imaging volume. The imposition of this constraint would sacrifice the simplicity and efficiency of our implementation. However, the positive definiteness constraint can be imposed when estimating the discrete diffusion tensor in each voxel with quadratic programming (24) or another constrained optimization scheme. In practice, this is seldom done because, at SNRs typical of most clinical DWI acquisitions, few diffusion tensors within an imaging volume are actually not positive definite. However, even if all the original discrete tensors are positive definite, the approximated or interpolated tensors are not guaranteed to be positive definite. Still, the continuous approximation of the tensor field, which spatially averages the discrete tensor data, tends to reduce the likelihood of observing nonpositive definite tensors compared to interpolation.



Gradient of the Isotropic Part of \mathbf{D}

FIG. 9. (a) An axial image of $\text{Trace}(\mathbf{D}(\mathbf{x}))$ in a normal subject. Juxtaposed in (b) is the corresponding image of the magnitude of the gradient of the isotropic part of the diffusion tensor field. Clearly visible are the boundaries between isotropic regions having different average diffusion properties, such as between brain parenchyma and CSF containing regions. Otherwise, the image has a relatively uniform intensity. The scale parameter used for these figures was 0.8. The “white” in (b) represents the value $1400 \mu\text{m}^2/\text{s}/\text{voxel}$ of the magnitude of the gradient while “black” is equal to 0.

In practice, instead of approximating the entire diffusion tensor field, we approximate its isotropic and anisotropic parts sequentially. This is because in homogeneous isotropic regions structure may be introduced where there is none. This is a curious but easily explained property of our continuous tensor field representation: in an homogeneous isotropic tensor field, only the isotropic part of the tensor field is continuous, while the anisotropic part is discontinuous. The tensor field approximation scheme, however, attempts to generate a continuous tensor field representation for both isotropic and anisotropic parts. In making the anisotropic part of the field continuous, complex artifactual structures are introduced, such as swirls, eddies, and coherent microdomains, which are not present in the original data. To remedy the problem, we first fit a continuous approximation to the isotropic part of $\mathbf{D}(\mathbf{x})$:

$$\underline{\mathbf{D}}(\mathbf{x})_{\text{iso}} = \langle \mathbf{D}(\mathbf{x}) \rangle \mathbf{I}. \quad [11]$$

Once calculated, we use it to approximate the remaining nor-

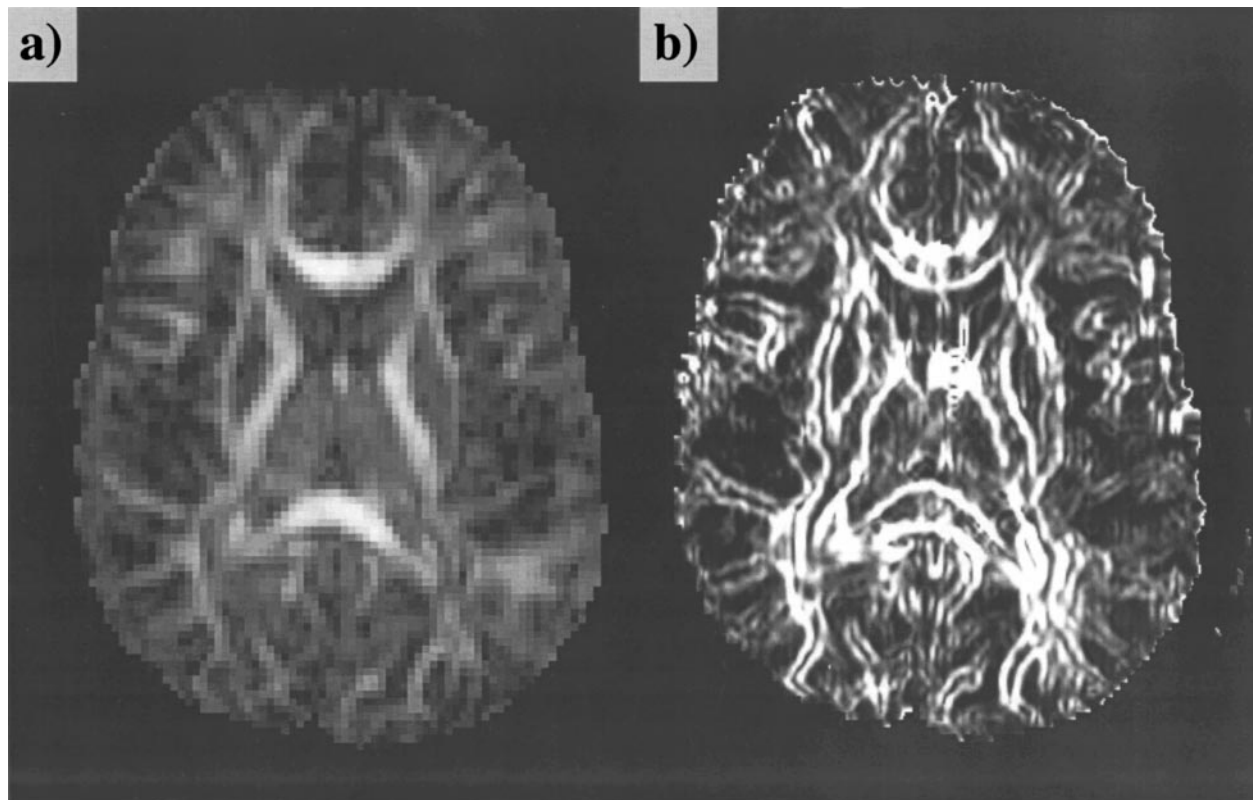
malized deviation tensor field:

$$\underline{\mathbf{D}}(\mathbf{x})_{\text{aniso}} = \left(\frac{1}{\langle \mathbf{D}(\mathbf{x}) \rangle} \right) (\underline{\mathbf{D}}(\mathbf{x}) - \langle \mathbf{D}(\mathbf{x}) \rangle \mathbf{I}). \quad [12]$$

In homogeneous isotropic regions, such as within normal tissue parenchyma, the isotropic part now appears uniform, whereas only at boundaries between parenchyma and CSF, such as in the ventricles, sulci, and gyri, are there significant spatial variations. Moreover, the anisotropic part is small in these regions.

In homogeneous anisotropic regions, the normalized anisotropic part is also quite uniform. Significant variations are seen at the boundaries of anisotropic regions, such as at the margins of the corpus callosum. We find no angular dependence in uniform tensor field patterns in which fibers are systematically rotated about the solid angle. This indicates that no orientational artifact was introduced by the approximation routine.

The heterogeneous anisotropic case offers intriguing possibilities for constructing tensor field templates whose fiber



Gradient of the Anisotropic Part of \mathbf{D}

FIG. 10. (a) A lattice anisotropy index axial image of a normal subject's brain. Juxtaposed in (b) is the corresponding image of the magnitude of the gradient of the anisotropic part of the diffusion tensor field. Note that the boundaries between white and gray matter are highlighted, but no signal is seen in CSF or in gray matter *per se*. Clearly visible are boundaries between regions of differing diffusion anisotropy, such as between coherent white matter tracts and brain parenchyma. The scale parameter used for these figures was 0.8. The "white" in (b) represents the value $1.5 \mu\text{m}^2/\text{s}/\text{voxel}$ of the magnitude of the gradient while "black" is equal to 0.

architecture is biologically relevant. These include tensor fields whose principal fiber axes are helically wound about a torus, like the muscle fibers of the heart (25, 26); "kiss" (i.e., approach each other) or cross, both of which are found in the optic chiasm; converge or diverge, such as in the pyramidal tract; and twist, bend, and/or circulate, such as in cortical white matter or in uterine smooth muscle.

The gradient of the isotropic part of $\mathbf{D}(\mathbf{x})$ identifies boundaries between homogeneous isotropic regions having different mean diffusivities, $\langle \mathbf{D}(\mathbf{x}) \rangle$, such as at boundaries between CSF and brain parenchyma at the margins of the ventricles, and in sulci and gyri. Since $\langle \mathbf{D}(\mathbf{x}) \rangle$ is approximately uniform within normal brain parenchyma (23, 27), we expect little variation in its gradient. However, one could speculate that in acute or chronic stroke, or in other clinical conditions in which the distribution of $\text{Trace}(\mathbf{D}(\mathbf{x}))$ changes within brain parenchyma, the gradient of the isotropic part of $\mathbf{D}(\mathbf{x})$ could help identify the borders of the affected territory.

On the other hand, simulations with template data suggest that the variation in the gradient of the deviation tensor should be small within relatively homogeneous isotropic regions, such

as in CSF and normal gray matter (in the absence of systematic artifacts), as well as in homogeneous anisotropic regions, such as in coherently organized white matter fiber tracts whose fiber direction is relatively uniform. We expect this quantity to be large, however, at the boundaries between coherently organized white matter and isotropic regions, where anisotropic diffusion properties are changing rapidly in space, and in regions where nerve fiber direction changes rapidly with position. We also expect this quantity to be large in regions where fibers cross, i.e., where powder averaging of the various underlying tensor fields reduces the measured diffusion anisotropy (4).

Thus, the gradient of the isotropic part of the diffusion tensor detects heterogeneity in isotropic regions, and the gradient of the anisotropic part of the diffusion tensor detects heterogeneity in anisotropic regions. Interestingly, while these quantities are based solely on algebraic and geometric features of the diffusion tensor field itself, they reflect distinct spatial variations in local tissue composition and microstructure.

Information about curvature could provide new information about development of nerve fiber tracts, the evolution of gyri and sulci during normal or abnormal development, and

possibly information about microstructural changes that may occur in neurodegenerative diseases. Without a method to provide a continuous approximation to the diffusion tensor field, the calculation of radius of curvature, mean curvature, or any other like parameters would not be practicable. Noise in the tensor field would be amplified by spatial differentiation rendering these quantities meaningless. Even so, as Fig. 7b indicates, calculated values of the curvature from the continuous tensor field can still be noisy and nonuniform in regions that are supposed to have uniform curvature. There are many mathematical complexities associated with obtaining proper estimates of curvature from the noisy diffusion tensor MRI data whose consideration is beyond the scope of this paper. A partial solution to this problem is to track a fiber and evaluate the curvature of this space curve using similar approximation methods, but now with a much larger scale factor. However, if the scaling factor used is $\Delta = 0.1$, which yields a great improvement in terms of the variance of the estimated curvature (Fig. 7c), changes of curvature on the order of 10 voxels would not be detectable. When used with *in vivo* DT-MRI data this can be a serious limitation.

In this work we also provide examples of certain differential variables that can be estimated using the continuous and smooth tensor field model. Taken together, DT-MRI parameters characterizing variations in the isotropic and anisotropic tensor fields can improve tissue segmentation by helping to better define boundaries between different tissue types, such as between white and gray matter. Still, we envision that by using our approximation method more sophisticated concepts and methods of differential geometry can now be developed and applied to the tissue segmentation problem.

Implications for Fiber Tractography

DT-MRI fiber tractography is a new method for following the trajectories of nerve and other fibrous tissues. Its underpinnings can be found in (15, 28–30). Recently, several groups have reported success in following fiber tracts and even individual fascicles on a gross anatomical length scale (7, 31–36). An assumption used in all these studies is that the eigenvector associated with the largest eigenvalue of the diffusion tensor is coincident with the vector tangent to the fiber tract (J). However, the discrete eigenvector field used to construct continuous fiber tracts is calculated from noisy DT-MRI data. Errors in the diffusion tensor field propagate as errors in the fiber tract direction field, $\varepsilon_1(x, y, z)$, from which fiber tract trajectories are calculated (7, 37, 38), as illustrated by the “cone of uncertainty” (37, 38). Conturo *et al.* interpolate noisy DWI data between voxels to increase the apparent resolution of their diffusion tensor data (31). We showed previously that interpolating DT-MRI data causes computed fiber tracts to swerve off course sooner than if the tensor field were approximated, since noise in DWIs introduces accumulated errors in the computed fiber tract trajectories (7). The methodology presented here is capable of generating a continuous, reduced-noise approximation to the measured DT-

MRI data that makes following coherently organized fiber tract more reliable and robust, as demonstrated in (7).

Microscopic (Underlying) Field vs Macroscopic (Voxel-Averaged) Field

The microscopic tensor field is one that describes water diffusion on a microscopic scale, whereas the measured effective tensor field describes the tensor field on a voxel-averaged macroscopic scale. If we assume no intercompartment mixing of spins, the measured macroscopic tensor field is a voxel average of this microscopic tensor field. While tense macro and micro fields should be similar in voxels containing tissue whose distribution of fiber directions is uniform, a significant disparity could exist between these fields in voxels whose distribution of fiber directions is nonuniform, such as regions where fibers diverge or converge (splay), bend or twist, branch or merge, etc. Generally, in these regions, the macroscopic field is a powder average of the heterogeneous microscopic tensor field within the voxel (4). An important long-term goal is to develop techniques to identify regions in which such powder averaging occurs, and infer the *microscopic* tensor field from these *macroscopic* voxel-scale measurements. Some progress has recently been reported in this area (39, 40).

This approximation treats discrete data as samples of the underlying continuous field. Although the DT-MRI data are voxel-averaged samples of the underlying field, these two data sets can be very different when the underlying field contains features that are on a scale finer than that of a single voxel. However, since we assume that the underlying diffusion tensor field is smooth (i.e., it changes on scales larger than a voxel), the difference between the voxel-averaged and point estimates is negligible. The shortcoming of this assumption is that it forces a prescribed degree of smoothness of the tensor field at sharp boundaries and interfaces. This explains why the “percent error maps” above show high intensity at borders between tissues, why borders appear somewhat enlarged, and in some cases, why tractography schemes that follow these smoothed tensor fields sometimes produce artifactual fiber trajectories (7). Work is underway to treat internal boundaries and piecewise discontinuities in the tensor field more naturally and robustly within the framework of this continuous tensor field approximation.

CONCLUDING REMARKS

This new methodology takes noisy, voxel-averaged, and discrete statistical samples of an underlying macroscopic effective diffusion tensor field as its input, and produces a continuous, smooth tensor field approximation as its output, specifically, approximated isotropic and anisotropic diffusion tensor fields. One of our essential findings is that the continuous tensor field representation can be constructed by performing repeated one-dimensional B-spline transforms of the DT-MRI data, greatly simplifying this complex task.

To test the fidelity of this approximation scheme, we developed a family of continuous tensor fields or templates, sampled them discretely, reconstructed a continuous field from these discrete data, and then compared the original and approximated tensor fields. We also tested the method's noise immunity by adding background noise to these templates using Monte Carlo methods. The templates are accurately reproduced except at boundaries where material properties change discontinuously or where the field is not microscopically homogeneous, such as in regions where fiber tracts cross, merge, etc. Besides being able to recover the original noiseless tensor field reliably, this approximation scheme substantially reduces the variance of quantities derived from DT-MRI. New MR parameters that characterize different structural and architectural features were proposed and displayed using *in vivo* DT-MRI data obtained from the human brain, which could not have been evaluated accurately from noisy DT-MRI data. This new methodology has already been successfully incorporated into a scheme for following nerve and other fiber tract trajectories *in vivo* (7).

APPENDIX

We describe the details of the implementation of the continuous tensor field approximation. The essential building block of our implementation is the optimal B -spline approximation in 1-D. It is based on a scale conversion algorithm which finds the optimal approximation to the original signal at a given scale Δ (13). The only difference in our implementation is the exclusion of the postfiltering step, as described in the block diagram of the algorithm in (13). Hence our model is determined once we obtain the optimal B -spline coefficients c_i . Below we describe how these coefficients are obtained and how they are used to represent $\mathbf{D}(\mathbf{x})$.

Optimal B -Spline Approximation in 1-D for an Arbitrary Scale Factor Δ

Let $s(k)$ be a discrete one-dimensional signal ($k \in \mathbb{Z}$, $s(k) \in l_2$) and $s^n(x)$ be the corresponding B -spline representation (interpolation) of the same signal in L_2 . These two are related through

$$s^n(x) = \sum_{k=-\infty}^{+\infty} c(k)\beta^n(x-k), \quad [\text{A.1}]$$

where $c(k) \in l_2$ are the B -spline coefficients and $\beta^n(x)$ is the B -spline of order n . The coefficients are obtained from the original signal $s(k)$ using a direct B -spline transform, which is a convolution operation of the original data with the appropriate filter (11, 12); i.e.,

$$c(k) = b_{INV}^n \otimes s(k), \quad [\text{A.2}]$$

where \otimes indicates the convolution operation and b_{INV}^n is the impulse response of the B -spline filter b^n (the samples of the

B -spline function of order n at integer values). Note that b_{INV}^n is the infinite impulse response (IIR) filter. Similarly, the discrete values of the interpolated signal, represented with B -spline coefficients $c(k)$, can be obtained through convolution, i.e., the indirect B -spline transform:

$$s(k) = b^n \otimes c(k). \quad [\text{A.3}]$$

In many situations, however, it can be advantageous to approximate the signal, rather than to interpolate it. In particular, if the original signal is noisy, introducing a smoothness constraint and approximating the data can be beneficial. We use a constraint that imposes the reduction of the space in which the signal is represented (effectively it is a constraint on the upper frequency bound). Thus, the desired transform is the one that yields the optimal B -spline coefficients representing the scaled down version of the signal through a relationship, similar to Eq. [A.1]; i.e.,

$$s_\Delta^n(x) = \sum_{k=-\infty}^{+\infty} c_\Delta(k)\beta^n(x\Delta-k). \quad [\text{A.4}]$$

One way to find the optimal B -spline coefficients, $c_\Delta(k)$, is to explicitly minimize the approximation error. Efficient algorithms can be designed based on this scheme (9, 11, 12); however, they are designed only for the cases where the scale parameter Δ is an integer. A more general approach is described in (13), in which the minimization task is modified and can be stated as follows: Given a function $f(x)$ in the original space S_x , find its minimum least square error approximation $f_\Delta(x)$ in the space scaled down by factor Δ , i.e., $S_{x\Delta}$. In this approach we equate $f(x)$ with the B -spline expansion of the original signal, i.e., $s^n(x)$, and similarly $f_\Delta(x)$ with $s_\Delta^n(x)$. Here the (approximately) optimal B -spline coefficients can be obtained for an arbitrary scale factor Δ . By projecting the $s^n(x)$ into the scaled space of $f_\Delta(x)$ we obtain the B -spline coefficients $c_\Delta(k)$ as

$$c_\Delta(k) = \Delta \langle s^n(x), \beta^n(x\Delta-k) \rangle, \quad [\text{A.5}]$$

where $\langle \cdot \rangle$ represents the inner product of two functions. Substituting $s^n(x)$ from Eq. [A.1] we obtain

$$c_\Delta(k) = \Delta \sum_{l=-\infty}^{\infty} c(l) \langle \beta^n(x-l), \beta^n(x\Delta-k) \rangle. \quad [\text{A.6}]$$

The inner product in Eq. [A.6], known as the sampling function, is a convolution of two B -splines and can be easily evaluated analytically for the piecewise constant and piecewise linear B -splines. However, for higher-order splines, approximate formulas described in (14) are used.

A general way of calculating the sampling function, which we use, is to perform the convolution in the Fourier domain, i.e., multiplication of the corresponding Fourier transforms of the

two splines. Note that this is also an approximate method since B -splines are bounded functions and their Fourier transforms are unbounded. The scaling function itself is bounded since it is a convolution of two bounded functions.

Although there are several approximations made in obtaining the B -spline coefficients, they are formal in nature. In practice the performance of this algorithm is nearly optimal. Once the B -spline coefficients, $c_{\Delta}(k)$, are determined we can obtain the continuous representation of the approximated signal at any point x using Eq. [4].

Multidimensional Approximation of Tensor Valued Functions

As already described under Theory, finding the tensor field representation could be reduced to finding a continuous representation of each of its individual tensor components (8) and letting the functions $b^i(\mathbf{x})$ which now serve as a basis for the components of the tensor field be a product of functions, i.e., $b^i(\mathbf{x}) = f^i(x)g^i(y)h^i(z)$. Since the basis functions are now separable, the task of finding the B -spline coefficients of the continuous model, $c_i(k, l, m)$, is reduced to sequentially applying Eq. [A.6] along the x , y , and z coordinates within the imaging volume for each tensor component. Consider a component of the diffusion tensor, $\mathbf{D}^i(\mathbf{x})$. The 1-D curves $\mathbf{D}^i(x, y_0, z_0)$ are processed along x for all discrete values, $y = y_0$ and $z = z_0$. The coefficients obtained in this first stage, $\mathbf{D}_{(c)}^i(k, y, z)$, are then similarly processed along y for all k_0 and z_0 , and then along z in a similar fashion. Ultimately, we obtain the desired coefficients, $c_i(k, l, m)$. Note that $c_i(k, l, m)$ corresponds to $c_{\Delta}(k)$ in the previous subsection on the 1-D approximation, i.e., the B -spline coefficients of the approximated signal. This avoids using the notation $c_{\Delta_1\Delta_2\Delta_3}^i(k, l, m)$.

Once the coefficients $c_i(k, l, m)$ are obtained, the tensor field can be determined at any point $\mathbf{x}(x, y, z)$ using Eq. [1]. Hence, the value of the tensor components at an arbitrary point $\mathbf{x}(x, y, z)$ can be expressed as

$$D_{xx}(\mathbf{x}) = \sum_{i,j,k} c_1(i, j, k)\beta^n(x\Delta_x - i)\beta^n(y\Delta_y - j)\beta^n(z\Delta_z - k)$$

⋮

[A.7]

$$D_{zz}(\mathbf{x}) = \sum_{i,j,k} c_6(i, j, k)\beta^n(x\Delta_x - i)\beta^n(y\Delta_y - j)\beta^n(z\Delta_z - k).$$

Although the summation extends over the whole range of indices, in practice, it is necessary to use only a small number of neighboring coefficients due to finite and small support of the B -spline functions. For the B -spline of order n , the range of indices needed to evaluate the function along one of the dimensions is $j_{min} = \lceil x - (n+1)/2 \rceil$, and $j_{max} = \lfloor x + (n+1)/2 \rfloor$, where $\lceil x \rceil$ ($\lfloor x \rfloor$) is the smallest (largest) integer greater (smaller) than x . For example, for the cubic spline, we need to sum over 4 indices in each dimension (total of 6×64 summands in

Eq. [A.7]). We usually choose the cubic B -splines. However, if the derivatives higher than second order are needed (e.g., calculation of the torsion of a curve requires the third-order derivative) we must use higher-order splines. Additionally, an advantage of using higher-order splines is that they improve separability properties of the derivatives, but at the expense of longer computation time. The evaluation of the derivatives of the tensor field is straightforward, since derivatives of the B -splines can be expressed recursively in terms of the B -splines or lower order using simple linear operations on B -spline coefficients (12).

Precompiled C-libraries of this implementation for several computer platforms and instructions for how to use them are available at <http://mscl.cit.nih.gov/spaj/dti/bcadt/>. These are also available by e-mail upon request to the authors.

ACKNOWLEDGMENTS

We thank Carlo Pierpaoli for providing DT-MR images that appear in this study using an approved NIH clinical protocol and for carefully reading this manuscript. We also thank Jeffrey Duda—a former summer student in our laboratory—for implementing early versions of several of these tensor field approximation algorithms in IDL.

REFERENCES

1. P. J. Basser, J. Mattiello, and D. Le Bihan, MR diffusion tensor spectroscopy and imaging, *Biophys. J.* **66**, 259–267 (1994).
2. P. J. Basser, Inferring microstructural features and the physiological state of tissues from diffusion-weighted images, *NMR Biomed.* **8**, 333–344 (1995).
3. P. J. Basser and C. Pierpaoli, Microstructural and physiological features of tissues elucidated by quantitative-diffusion-tensor MRI, *J. Magn. Reson. B* **111**, 209–219 (1996).
4. C. Pierpaoli and P. J. Basser, Toward a quantitative assessment of diffusion anisotropy [published erratum appears in *Magn. Reson. Med.* **37**, 972 (1997)], *Magn. Reson. Med.* **36**, 893–906 (1996).
5. P. J. Basser, New histological and physiological stains derived from diffusion-tensor MR images, *Ann. N.Y. Acad. Sci.* **820**, 123–138 (1997).
6. P. J. Basser, S. Pajevic, C. Pierpaoli, J. Duda, and A. Aldroubi, Fiber-tractography in human brain using diffusion tensor MRI (DT-MRI), 8th Annual ISMRM, Denver, CO, p. 784, 2000.
7. P. J. Basser, S. Pajevic, C. Pierpaoli, J. Duda, and A. Aldroubi, In vivo fiber-tractography in human brain using diffusion tensor MRI (DT-MRI) data, *Magn. Reson. Med.* **44**, 625–632 (2000).
8. A. Aldroubi and P. J. Basser, Reconstruction of vector and tensor fields from sampled discrete data, in “Contemporary Mathematics” (L. W. Baggett and D. R. Larson, Eds.), pp. 1–15, Amer. Math. Soc., Providence, RI (1999).
9. A. Aldroubi, Oblique projections in atomic spaces, *Proc. Amer. Math. Soc.* **124**, 2051–2060 (1996).
10. S. Pajevic and P. J. Basser, Parametric description of noise in diffusion tensor MRI, 8th Annual Meeting of the ISMRM, Philadelphia, PA, p. 1787, 1999.
11. M. Unser, A. Aldroubi, and M. Eden, B-spline signal processing. Part I. Theory, *IEEE Trans. Signal Process.* **41**, 821–833 (1993).
12. M. Unser, A. Aldroubi, and M. Eden, B-spline signal processing. Part II. Efficient design and implementation, *IEEE Trans. Signal Process.* **41**, 834–848 (1993).
13. M. Unser, A. Aldroubi, and M. Eden, Enlargement or reduction of digital images with minimum loss of information, *IEEE Trans. Image Process.* **4**, 247–258 (1995).

14. A. Aldroubi, M. Eden, and M. Unser, Discrete spline filters for multiresolutions and wavelets of 12, *SIAM Math. Anal.* **25**, 1412–1432 (1994).
15. P. J. Basser, Fiber-tractography via diffusion tensor MRI (DT-MRI), 6th ISMRM, Sydney, Australia, p. 1226, 1998.
16. R. M. Henkelman, Measurement of signal intensities in the presence of noise in MR images, *Med. Phys.* **12**, 232–233 (1985).
17. A. Virta, A. Barnett, and C. Pierpaoli, Visualizing and characterizing white matter fiber structure and architecture in the human pyramidal tract using diffusion tensor MRI, *Magn. Reson. Imaging* **17**, 1121–1133 (1999).
18. P. J. Basser, J. Mattiello, and D. Le Bihan, Estimation of the effective self-diffusion tensor from the NMR spin echo, *J. Magn. Reson. B* **103**, 247–254 (1994).
19. J. Mattiello, P. J. Basser, and D. Le Bihan, Analytical expression for the b matrix in NMR diffusion imaging and spectroscopy, *J. Magn. Reson. A* **108**, 131–141 (1994).
20. J. Mattiello, P. J. Basser, and D. Le Bihan, The b matrix in diffusion tensor echoplanar imaging, *Magn. Reson. Med.* **37**, 292–300 (1997).
21. R. W. Hamming, “Digital Filters,” Prentice Hall, Englewood Cliffs, NJ (1983).
22. P. M. Morse and H. Feschbach, “Methods of Theoretical Physics,” McGraw–Hill, New York (1953).
23. C. Pierpaoli, P. Jezzard, P. J. Basser, A. Barnett, and G. Di Chiro, Diffusion tensor MR imaging of the human brain, *Radiology* **201**, 637–648 (1996).
24. E. T. Ahrens, D. H. Laidlaw, C. Readhead, C. F. Brosnan, S. F. Fraser, and R. E. Jacobs, MR microscopy of transgenic mice that spontaneously acquire experimental allergic encephalomyelitis, *Magn. Reson. Med.* **40**, 119–132 (1998).
25. D. D. J. Streeter, W. E. Powers, M. A. Ross, and F. Torrent-Guasp, Three-dimensional fiber orientation in the mammalian left ventricular wall, in “Cardiovascular System Dynamics” (J. Baan, A. Noordegraaf, and J. Raines, Eds.), pp. 73–84, MIT Press, Cambridge, MA (1978).
26. D. D. J. Streeter, H. M. Spotnitz, D. P. Patel, J. J. Ross, and E. H. Sonnenblick, Fiber orientation in the canine left ventricle during diastole and systole, *Circ. Res.* **24**, 339–347 (1969).
27. A. M. Ulug, N. Beauchamp, R. N. Bryan, and P. C. M. van Zijl, Absolute quantitation of diffusion constants in human stroke, *Stroke* **28**, 483–490 (1997).
28. P. J. Basser and D. Le Bihan, Fiber orientation mapping in an anisotropic medium with NMR diffusion spectroscopy, 11th Annual Meeting of the SMRM, Berlin, p. 1221, 1992.
29. P. J. Basser and B. J. Roth, Stimulation of a myelinated nerve axon by electromagnetic induction, *Med. Biol. Eng. Comput.* **29**, 261–268 (1991).
30. V. J. Wedeen, T. L. Davis, R. M. Weisskoff, R. Toottell, B. R. Rosen, and J. W. Belliveau, White matter connectivity explored by MRI, Proceedings of the First International Conference for Functional Mapping of the Human Brain, Paris, p. P1.36, 1995.
31. T. E. Conturo, N. F. Lori, T. S. Cull, E. Akbudak, A. Z. Snyder, J. S. Shimony, R. C. McKinstry, H. Burton, and M. E. Raichle, Tracking neuronal fiber pathways in the living human brain, *Proc. Natl. Acad. Sci. U.S.A.* **96**, 10422–10427 (1999).
32. D. K. Jones, A. Simmons, S. C. Williams, and M. A. Horsfield, Non-invasive assessment of axonal fiber connectivity in the human brain via diffusion tensor MRI, *Magn. Reson. Med.* **42**, 37–41 (1999).
33. D. K. Jones, S. C. R. Williams, and M. A. Horsfield, Full representation of white-matter fiber direction on one map via diffusion tensor analysis, 5th ISMRM Meeting, Vancouver, p. 1743, 1997.
34. S. Mori, R. Xue, B. Crain, M. Solaiyappan, V. P. Chacko, and P. C. M.v. Zijl, 3D reconstruction of axonal fibers from diffusion tensor imaging using fiber assignment by continuous tracking (FACT), 8th Annual Meeting of the ISMRM, Philadelphia, PA, p. 320, 1999.
35. S. Mori, B. J. Crain, V. P. Chacko, and P. C. van Zijl, Three-dimensional tracking of axonal projections in the brain by magnetic resonance imaging, *Ann. Neurol.* **45**, 265–269 (1999).
36. C. Poupon, C. A. Clark, V. Frouin, I. Bloch, D. Le Bihan, and J.-F. Mangin, Tracking white matter fascicles with diffusion tensor imaging, 8th Annual Meeting of the ISMRM, Philadelphia, PA, p. 325, 1999.
37. P. J. Basser and S. Pajevic, Statistical artifacts in diffusion tensor MRI (DT-MRI) caused by background noise, *Magn. Reson. Med.* **44**, 41–50 (2000).
38. P. J. Basser, Quantifying errors in fiber direction and diffusion tensor field maps resulting from MR noise, 5th Scientific Meeting of the ISMRM, Vancouver, p. 1740, 1997.
39. E. L. Bossart, B. A. Inglis, D. L. Buckley, E. D. Wirth III, and T. H. Mareci, Multiple component diffusion tensor imaging in excised fixed CNS tissue, ISMRM, Philadelphia, PA, p. 328, 1999.
40. D. S. Tuch, R. M. Weisskoff, J. W. Belliveau, and V. J. Wedeen, High angular resolution diffusion imaging of the human brain, ISMRM, Philadelphia, PA, p. 321, 1999.